Microfluidic gas flow profiling using remote detection NMR

Christian Hilty*[†], Erin McDonnell[†], Josef Granwehr[†], Kimberly Pierce[†], Song-I Han[†‡], and Alexander Pines[†]

[†]Lawrence Berkeley National Laboratory, Materials Sciences Division, and University of California Berkeley, Department of Chemistry, Berkeley CA 94720, USA

[‡]Present address: Department of Chemistry and Biochemistry, University of California Santa Barbara, CA 93106-9510, USA

*To whom correspondence should be addressed. E-mail: hilty@berkeley.edu

Classification: Physical Sciences, Applied Physical Sciences

Number of text pages: 13

Number of words in abstract: 92

Number of characters in paper: 32100

(including Fig1: 7cm / 1 col. = 1380 char.; Fig. 2: 10cm / 1 col. = 1920 char.; Fig. 3: 5cm / 2 col. = 2040 char.; Fig. 4: 13.5cm / 2 col. = 5100 char.)

Abstract

We have used Nuclear Magnetic Resonance (NMR) to obtain spatially and temporally resolved profiles of gas flow in microfluidic devices. Remote detection of the NMR signal both overcomes the sensitivity limitation of NMR, and enables time-of-flight measurement in addition to spatially resolved imaging. Thus, detailed insight is gained into the effects of flow, diffusion and mixing in specific geometries. The ability for non-invasive and tracer-free measurement of microfluidic flow of both gases and liquids is unique to this approach and is important for the design and the operation of microfluidic devices.

Introduction

Miniaturized fluid handling devices have recently attracted considerable interest in many areas of science (1). Such microfluidic chips perform a variety of functions, ranging from analysis of biological macromolecules (2, 3) to catalysis of reactions and sensing in the gas phase (4, 5). To enable precise fluid handling, accurate knowledge of the flow properties within these devices is important. Due to low Reynolds numbers, laminar flow is usually assumed. However, either by design or unintentionally, the flow characteristic in small channels is often altered, for example by surface interactions, viscous and diffusional effects, or electrical potentials. Therefore, its prediction is not always straight-forward (6-8). Currently, most microfluidic flow measurements rely on optical detection of markers (9, 10), requiring the injection of tracers and transparent devices. Here, we show profiles of microfluidic gas flow in capillaries and chip devices obtained by NMR in the remote detection modality (11, 12). Through the transient measurement of dispersion (13), NMR is well adaptable for non-invasive, yet sensitive

determination of the flow field and provides a potentially more powerful tool to profile flow in capillaries and miniaturized flow devices.

NMR remote detection separates the encoding of NMR information from the detection of the actual signal. Information about a stationary object of interest is encoded into spin polarization of a mobile sensor using radio-frequency (rf) pulses and field gradients. The spin sensor is then physically transferred to a different location for detection. This leads to a decisive enhancement of signal in cases where geometrical constraints prevent the use of a sensitive NMR coil for detection directly at the sample site (11, 12). In the present work, we studied gas flow in model microfluidic devices, using hyperpolarized ^{129}Xe as a spin carrying nucleus (14).

Experimental Procedures

Image information was encoded with an rf coil that completely encompassed the microfluidic device (Fig. 1). Such a coil arrangement ideally allows NMR image information to be obtained from the entire microfluidic device, and for measuring flow provides a decisive advantage over localized detection achievable for example with microfabricated surface coils (15). However, the low filling factor on the order of 10^{-5} severely limits the obtainable signal and makes the acquisition of an NMR spectrum or image of gas in the conventional way unviable. With remote detection, the outflow of the fluid from the device can be utilized to carry the encoded information into a micro solenoid coil (16) wound around a capillary, which is connected to the outlet of the microfluidic device. The microcoil has a superior filling factor and is ideally suited to remotely retrieve the previously encoded information with a sensitivity gain of several orders of magnitude (17). Furthermore, remote detection uniquely provides the

possibility to obtain the axial dispersion of the fluid as an additional experimental dimension by recording the time-of-flight (TOF) between encoding and detection of individual spin packets. Thereby, the encoded signal is read out in a time-dependent manner (13), showing how fluid spreads as it travels through the device. The NMR pulse sequence for the acquisition of these dispersion resolved images is based on phase encoded imaging (18) in the encoding coil, while a stroboscopic signal detection scheme is applied on the microcoil to read out the axial dispersion (Fig.2). The encoding step thus tags the fluid in a spatially dependent way, without the need to physically insert a marker. Nuclear spins are ideal tracers, as they are naturally present in the fluid, and their state does not influence the flow properties in any way.

Results and Discussion

Fig. 3A shows the *z*-profile of gas flowing from top to bottom through a straight capillary with 150 μm inner diameter, as a function of the TOF between encoding and detection. Immediately apparent is its slope, which represents the mean flow velocity inside the capillary, $v \approx 55\ \mathrm{cm \cdot s^{-1}}$. The axial dispersion of the flow appears very small, as evidenced by a narrow distribution of travel times for any tagging location along the *z* direction. This suggests a plug flow-like behavior and may at first glance appear contradictory to the expected laminar flow profile at a low Reynolds number of less than 10. However, this flow characteristic can be explained by the fast lateral diffusion of individual gas molecules, which diffuse across the channel in a very short time, and efficiently sample all streamlines. The calculated (19, 20) and by pulsed field gradient NMR (21) experimentally determined diffusion constant of D=0.06 $\mathrm{cm^2 \cdot s^{-1}}$ for ^{129}Xe at the given conditions translates to an average molecular displacement across 100 μm in

approximately 800 μs. The resulting dispersion profile reflects the combined effects of the laminar flow properties and lateral diffusion across the channel, which is fast compared to the total time of flight between the encoding and detection location. This emphasizes the importance of experimental techniques to understand characteristic flow patterns in microfabricated channels or networks.

Figs. 3B and C show profiles of axial dispersion, which were obtained from a microfluidic glass chip with channels etched to a depth of 50 μm. The chip by design contains an enlargement of the channel width (*x* direction), but not of the depth. Its geometry was chosen to serve as a model for a microfluidic NMR sensor, which could in the future be surface-activated by chemical or biological means. Between the two profiles, the chip geometry differs in that the chip in c contained a mixing volume of 900 nl at the channel outlet (marked with a large open circle), which was not present in the chip in b. The comparison between the two profiles demonstrates that this geometric difference leads to very distinct flow properties, which are discussed below. The inlet and outlet capillaries, with 150 μm inner diameter, were inserted perpendicular to the plane of the chip, therefore they contained a short loop, which is seen at travel times below 275 ms. At travel times above this value the gas flowing inside the microfluidic chip is visible. In b, the different flow velocities in the narrow (travel times 350–425 ms) and wide (425–700 ms) sections of the device can directly be observed due to the different slopes of the trace in the profile. Above 775 ms, gas that remains for a long time in a mixing volume at the site of the connection to the inlet capillary can be observed. In contrast, in c, a substantial residence time is seen at the outlet mixing volume as well. Moreover, the signal shows a forking at a travel time of 350 ms, with one branch being fed from the enlarged section of the channel as in b, and the other

branch due to gas residing longer in the mixing volume. By measuring the length of the residence time until the forking occurs, and the flow velocity, one can estimate the outlet volume that is effectively connected to the flow field to be about 600 nl. Thus, the volume that gets exchanged only slowly, which is responsible for the stationary branch of the fork, is about 300 nl. This emphasizes the complementary character of direct flow imaging (22-25) and TOF flow imaging. The former provides a map of local velocity vectors, while the latter is able to distinguish between different flow paths and shows how well a certain volume element is connected to the flow field. The smaller this connection is, the broader the dispersion profile and the weaker the signal becomes. Flow profiles containing multiple spatial dimensions can be recorded by extending the experimental scheme described above to include pulsed field gradients along multiple axes. Because of the two-dimensional nature of the device used in Fig. 3B, an additional dataset was recorded with spatial resolution along *x* and *z*. With the TOF dimension available from the remote detection scheme, this results in a three-dimensional data set. The five panels of Fig. 4A present a selection of images taken from this dataset for different times of travel. Each panel is an image showing the spatially resolved origin of an ensemble of spins arriving in the detection coil at one time. The leftmost panel with the shortest travel time, 470 ms, shows gas that was close to the outlet of the chip during encoding. Subsequently, gas flowing through the enlarged center section of the chip is seen, while the rightmost panels contain intensity originating close to the inlet of the chip. A comparison reveals several details about the gas flow inside of the chip. For example, the first image shown from the wide section of the chip (540 ms) has a flat profile, while the second image (610 ms) clearly shows a curvature of the profile across the channel, with the points containing intensity close to x=±1 mm located further down

in the channel than intensity-containing points close to x=0 mm, which arises due to a difference in TOF between gas close to the edge (x= ±1 mm) and the center section (x=0 mm). This is indicative of a non-uniform velocity field inside the chip, which is not effectively mixed by transverse diffusion along the x-dimension over the time scale of the gas flow through the chip. In the image of the position where the channel widens (680 ms), a non-uniform signal distribution is apparent, with a maximum at x=0 and z=3.5 cm and weaker intensity closer to the outlet and towards the edges. This suggests that a certain fraction of gas from the section in the center of the channel reaches the outlet faster than average. Furthermore, when comparing this image with the image where the channel narrows again (540 ms), it can be seen that gas spreads into the wide section (z=3.5 cm) less rapidly than it condenses back into the narrow section (z=2.5 cm). At z=3.5 cm, the edges of the widening channel contain no intensity, indicating that gas in these locations is less efficiently replaced. This may be even more easily visible in Fig. 4B, where a sum of the intensity over all times of travel is shown. The effect of axial dispersion arising due to the flow properties inside of the chip is also readily visible when looking at time-resolved traces of gas originating from a specific position as it arrives at the detection coil. Fig. 4C shows three traces for gas inside of the microfluidic chip at different z-positions. The amount of axial dispersion as the gas flows within the enlarged section of the chip is immediately apparent from the increasing width and decreasing height of the peaks for increasing distances to the outlet.

These results illustrate the ability to non-invasively study flow properties inside of microfluidic devices by NMR with time-of-flight imaging. We profiled microfluidic gas flow, which was enabled despite the low spin-density in a gas by using remote detection

and hyperpolarized xenon as spin carrying tracer. A further improvement of the sensitivity up to 2-3 orders of magnitude could be achieved by increasing the concentration of ^{129}Xe (26), and by using a polarizer optimized for low mass flow (27). The same experiments can also be performed with liquids, such as water and many organic solvents, where nuclear spins that are already present in the liquid can be tagged during encoding. NMR provides several advantages compared to other methods for flow measurements, including freedom in the choice of the flow medium and the ability to work with opaque devices. With remote time-of flight imaging, foreign tracer substances that may otherwise be needed are not required, and microfluidic devices do not need to be specifically designed for NMR detection. The obtained axial dispersion profiles represent global characteristics of the entire flow path, which allows observing properties of the flow even when imaging with moderate spatial resolution compared to the channel size. In contrast to local velocity profiles, this shows how individual points inside a microfluidic device are connected to the flow field, and novel information is obtained about fluid velocities, mixing properties, and dispersion.

Acknowledgement

This work was supported by the Director, Office of Science, Office of Basic Energy Sciences, Materials Sciences and Engineering Division, of the U.S. Department of Energy under Contract No. DE-AC03-76SF00098. C.H. acknowledges support from the Schweizerischer Nationalfonds through a post-doctoral fellowship. Microfabrication was done in the Berkeley Microlab. We thank Dr. Mahua Hajra for help with microfabrication, and Prof. Mathies for useful discussions.

References

1. Chovan, T. & Guttman, A. (2002) *Trends Biotechnol.* **20,** 116-122.
2. Burns, M. A., Johnson, B. N., Brahmasandra, S. N., Handique, K., Webster, J. R., Krishnan, M., Sammarco, T. S., Man, P. M., Jones, D., Heldsinger, D., Mastrangelo, C. H. & Burke, D. T. (1998) *Science* **282,** 484-487.
3. Huber, D. L., Manginell, R. P., Samara, M. A., Kim, B. I. & Bunker, B. C. (2003) *Science* **301,** 352-354.
4. Ueno, Y., Horiuchi, T., Morimoto, T. & Niwa, O. (2001) *Anal. Chem.* **73,** 4688-4693.
5. Kobayashi, J., Mori, Y., Okamoto, K., Akiyama, R., Ueno, M., Kitamori, T. & Kobayashi, S. (2004) *Science* **304,** 1305-1308.
6. Pathak, J. A., Ross, D. & Migler, K. B. (2004) *Phys. Fluids* **16,** 4028-4034.
7. Johnson, T. J., Ross, D. & Locascio, L. E. (2002) *Anal. Chem.* **74,** 45-51.
8. Stone, H. A., Stroock, A. D. & Ajdari, A. (2004) *Annu. Rev. Fluid Mech.* **36,** 381-411.
9. Singh, A. K., Cummings, E. B. & Throckmorton, D. J. (2001) *Anal. Chem.* **73,** 1057-1061.
10. Devasenathipathy, S., Santiago, J. G. & Takehara, K. (2002) *Anal. Chem.* **74,** 3704-3713.
11. Moulé, A. J., Spence, M. M., Han, S. I., Seeley, J. A., Pierce, K. L., Saxena, S. & Pines, A. (2003) *Proc. Natl. Acad. Sci. USA* **100,** 9122-9127.
12. Seeley, J. A., Han, S. I. & Pines, A. (2004) *J. Magn. Reson.* **167,** 282-290.
13. Granwehr, J., Harel, E., Han, S., Garcia, S., Sen, P. N., Song, Y. Q. & Pines, A. (2005) *submitted*.

14. Walker, T. G. & Happer, W. (1997) *Rev. Mod. Phys.* **69,** 629-642.

15. Massin, C., Boero, C., Vincent, F., Abenhaim, J., Besse, P. A. & Popovic, R. S. (2002) *Sensor Actuat. A-Phys.* **97-8,** 280-288.

16. Olson, D. L., Peck, T. L., Webb, A. G., Magin, R. L. & Sweedler, J. V. (1995) *Science* **270,** 1967-1970.

17. McDonnell, S., Han, S. I., Hilty, C., Pierce, K. & Pines, A. (2005) *submitted*.

18. Callaghan, P. T. (1991) *Principles of Nuclear Magnetic Resonance Microscopy* (Oxford University Press, New York).

19. Hirschfelder, J. O., Curtiss, C. F. & Bird, R. B. (1954) *Molecular theory of gases and liquids* (Wiley, New York).

20. Reid, R. C., Prausnitz, J. M. & Sherwood, T. K. (1977) *The properties of gases and liquids* (McGraw-Hill, New York).

21. Stejskal, E. O. & Tanner, J. E. (1965) *J. Chem. Phys.* **42,** 288-292.

22. Kaiser, L. G., Logan, J. W., Meersmann, T. & Pines, A. (2001) *J. Magn. Reson.* **149,** 144-148.

23. Koptyug, I. V., Altobelli, S. A., Fukushima, E., Matveev, A. V. & Sagdeev, R. Z. (2000) *J. Magn. Reson.* **147,** 36-42.

24. Codd, S. L., Manz, B., Seymour, J. D. & Callaghan, P. T. (1999) *Phys. Rev. E* **60,** R3491-R3494.

25. Zhang, X. F. & Webb, A. G. (2005) *Anal. Chem.* **77,** 1338-1344.

26. Mortuza, M. G., Anala, S., Pavlovskaya, G. E., Dieken, T. J. & Meersmann, T. (2003) *J. Chem. Phys.* **118,** 1581-1584.

27. Knagge, K., Prange, J. & Raftery, D. (2004) *Chem. Phys. Lett.* **397,** 11-16.

Figure Legends

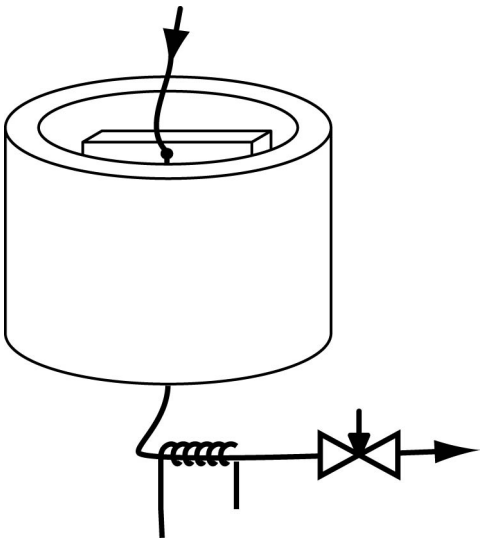

Fig. 1. Experimental setup for flow dispersion measurements. Pressurized hyperpolarized xenon gas mixture containing 0.3% NMR active ^{129}Xe (1% Xe at natural isotope abundance, 10% N_2, 89% He at 5.6 atm delivery pressure), spin-polarized to 10%, is supplied from the top. It flows via a capillary through the microfluidic device to be profiled, and exits at the bottom. The entire microfluidic device is surrounded by an assembly of magnetic field gradient and radio-frequency coils (3 cm × 4.5 cm) for encoding, while the outlet capillary leads through a microsolenoid (3 mm long, 400 μm inner diameter) for remote signal detection. The flow rate is controlled by an adjustable constriction at the outlet. The whole apparatus is inserted into the bore of a superconducting magnet (7 T).

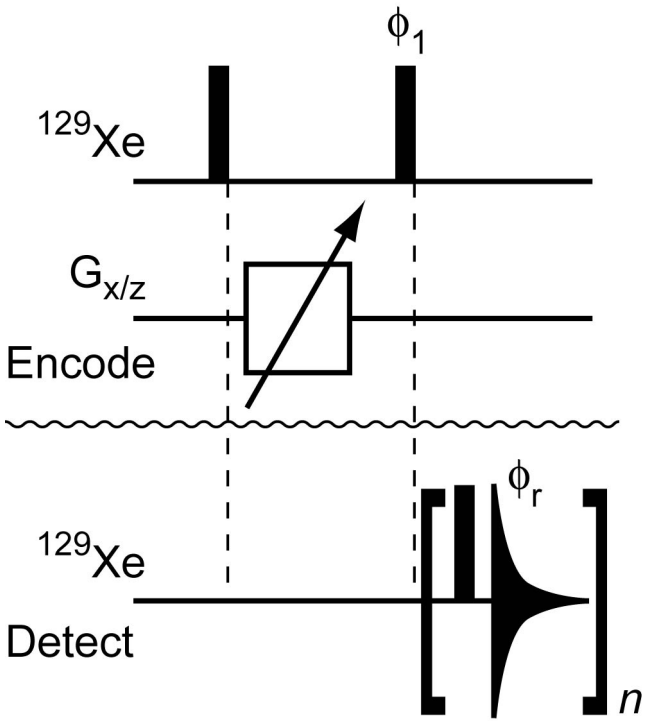

Fig. 2. Pulse sequence used for remote imaging of microfluidic flow. The top ^{129}Xe line and the line labeled $G_{x/z}$ show RF pulses at the frequency of ^{129}Xe and gradient pulses along the *x* and *z*-axis, respectively, which are applied to the encoding volume. The pulse sequence elements applied to the detection microcoil are shown on the lower ^{129}Xe line. Black bars represent 90° pulses, and the triangular shape symbolizes acquisition of one free induction decay (FID). Phases are x, unless otherwise noted; $\phi_1 = \phi_r = \{x, y, -x, -y\}$. On the encoding coil, the 90° pulse length is 90 μs, and the carrier frequency is set on-resonance with respect to the frequency of Xe gas. Gradient pulses are applied for 200 μs, with an additional recovery time of 10 μs. The gradient strength is varied in an array of otherwise identical experiments to obtain phase encoded image information. On the encoding coils, the first rf pulse is for excitation, the gradient pulses encode the image in a phase encoded manner, and the second rf pulse stores the obtained intensity as longitudinal coherence. For experiments with one spatial dimension, gradients are applied along both the *x* and *z* axes, whereby for each *x*

gradient value, all *z* gradient values are used. On the detection microcoil, the 90° pulse length is 0.65 μs, and the carrier frequency is set 7 kHz off-resonance with respect to the frequency of Xe gas, in order to avoid zero-frequency artifacts. The acquisition length for one single free induction decay determines the time resolution of the flow profiles, and is set at or below the residence time of gas in the detection coil. The number of repetitions, *n*, is set so that the total acquisition time exceeds the longest time of travel of gas between the encoding and detection volumes. The flow profile, which is a spatially resolved image in function of time of flight between the locations of encoding and detection, is obtained by applying a complex Fourier transformation to each acquired FID, integrating the real and imaginary part of each peak volume, and using the integrals corresponding to the same time of travel, but different gradient strengths for a second complex Fourier transformation.

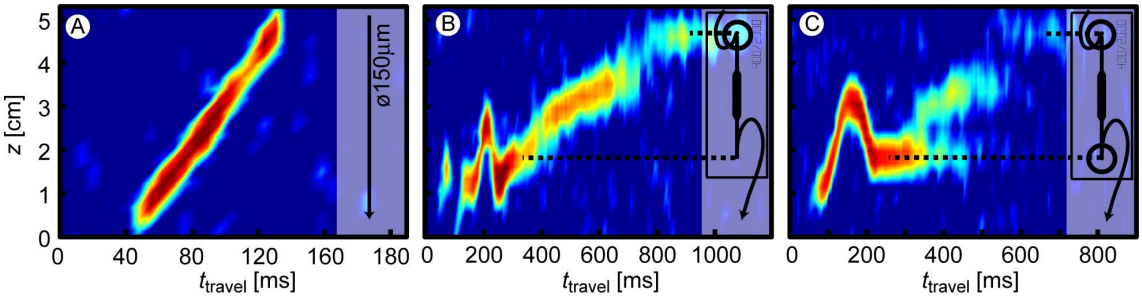

Fig. 3. Profiles of axial microfluidic flow dispersion. (*A*) Profile resolved in time of travel between the encoding and detection coil, and along the *z*-axis parallel to the magnetic field, obtained from a capillary with 150 µm inner diameter. (*B*) Profile from a model microfluidic chip device containing a channel enlargement, directly connected to a capillary. (*C*) Profile from the same microfluidic chip connected to a capillary via a cylindrical volume of 900 nl. The gas was flowing in the direction of the negative *z*-axis, with a flow rate set to ~2.5 ml·min^{-1} (STP), and a delivery pressure of 5.6 atm. The chip used in B and C consists of a channel that is 50 µm deep and 30 mm long. It is 400 µm wide at both ends, but is enlarged to a width of 2000 µm in the center. The positions along the long axis corresponding to the inlet and outlet of the chip are highlighted with dashed lines. Cavities with a volume of 900 nl between chip and capillary are marked with a large open circle in the drawings. Images were acquired in 3h with a spatial resolution of 5.3 mm and a time resolution of 6 ms.

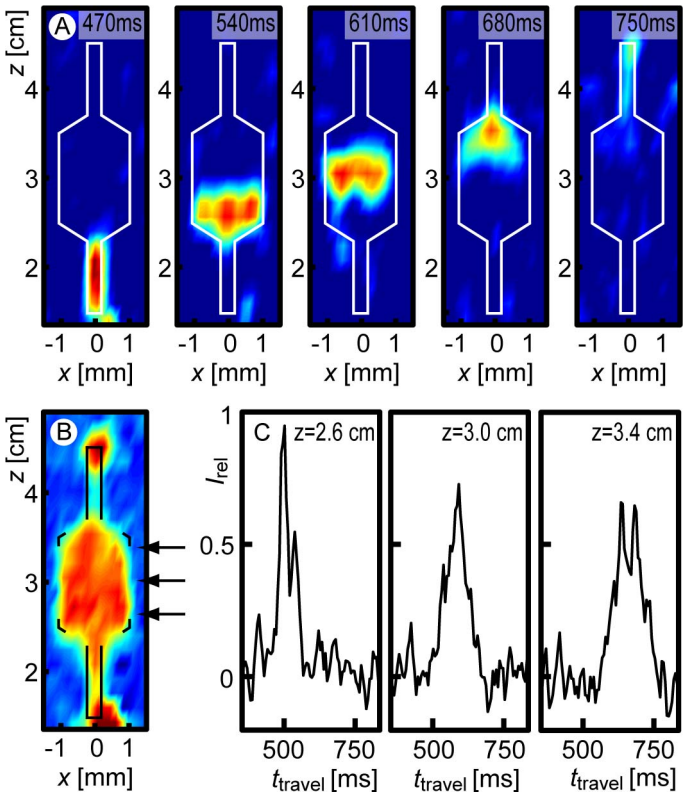

Fig. 4. Microfluidic flow resolved in two spatial dimensions along the *x* and *z* axes. (*A*) Five panels with images of gas originating in the microfluidic chip (outlined in white), shown for gas flowing from top to bottom, for different times of travel between the encoding location and detection coil. (*B*) Image of the perfused areas in the chip, reconstructed by summing the data shown in A over all travel times; A, three dispersion curves for gas originating at different *z*-positions and *x*=0 within the wide section of the chip. The positions of the traces in **c** are indicated with arrows in B. The data was recorded in 9 h with a spatial resolution of 340 µm along the *x*-direction, and 2.7 mm along the *z*-direction, using the same chip as in Fig. 3B.